Accelerated creep in solid oxide fuel cell anode supports during reduction

Frandsen, Henrik Lund; Makowska, Malgorzata Grazyna; Greco, Fabio; Chatzichristodoulou, Christodoulos; Ni, De Wei; Curran, Declan; Strobl, M.; Kuhn, Luise Theil; Hendriksen, Peter Vang

Published in:
Journal of Power Sources

Link to article, DOI:
10.1016/j.jpowsour.2016.04.097

Publication date:
2016

Document Version
Peer reviewed version

Accelerated creep in solid oxide fuel cell anode supports during reduction

H. L. Frandsen[1], M. Makowska[1,2], F. Greco[1], C. Chatzichristodoulou[1], D. W. Ni[1], D. J. Curran[1], M. Strobl[2], L. Theil Kuhn[1], P. V. Hendriksen[1]*

[1]Department of Energy Conversion and Storage, Technical University of Denmark, Roskilde, Denmark.

[2] European Spallation Source AB, Science Division, Lund, Sweden.

Abstract

To evaluate the reliability of solid oxide fuel cell (SOFC) stacks during operation, the stress field in the stack must be known. During operation the stress field will depend on time as creep processes relax stresses. The creep of reduced Ni-YSZ anode support at operating conditions has been studied previously. In this work a newly discovered creep phenomenon taking place during the reduction is reported. This relaxes stresses at a much higher rate (~×10^4) than creep during operation. The phenomenon was studied both in three-point bending and uniaxial tension. Differences between the two measurements could be explained by newly observed stress promoted reduction. Finally,

[*] Corresponding author:

E-mail: hlfr@dtu.dk,

Address: Frederiksborgvej 399, DK-4000 Roskilde, Denmark,

Phone: +45 46 77 56 68, Fax: +45 46 77 58 58

samples exposed to a small tensile stress (~0.004 MPa) were observed to expand during reduction, which is in contradiction to previous literature. These observations suggest that release of internal residual stresses between the NiO and the YSZ phases occurs during reduction. The accelerated creep should practically eliminate any residual stress in the anode support in an SOFC stack, as has previously been indirectly observed. This phenomenon has to be taken into account both in the production of stacks and in the simulation of the stress field in a stack based on anode supported SOFCs.

Keywords: Creep, reduction, SOFC, SOEC, Ni-YSZ, chemo-mechanical coupling

1. Introduction

With the utilization of the solid oxide fuel cells (SOFCs) in stacks and systems, their reliability has received increasing attention. In order to minimize the risk of failure by design or suitable operation, the stresses under operation of the SOFC stacks must be assessed together with the material resistance to failure. If fracture mechanics is employed, fracture toughnesses needs to be measured, see e.g. [1-3], and if a statistical approach is applied, one needs to assess the distribution of the strength of the brittle components at operational conditions [4-7]. Often the statistical approach is preferred as it offers simpler experiments and stress analyses, see e.g. [8-11].

The stress field at a given time during operation is influenced by external loads, the thermal field from the operation, thermal expansion coefficients, chemical expansions, the particular design of the stack components, the mechanical material properties but also the full thermo-mechanical history until the given time, see e.g. [9-12]. The residual stresses relevant during operation depend on the stack assembly procedure (e.g. sintering temperature of the cell, stack assembly temperature, etc.) but also on the time at high temperature as the stresses relax over time by creep processes.

In general detrimental failure of the SOFC stacks can be expected if cracks through the electrolyte develop, although minor cracks might be tolerable under constant operation. To avoid cracking the stress level in all the cell layers must be kept well below the strength of the respective cell layers, due to the statistical distribution of strength and cracks induced by slow crack growth. In this context the creep of all the cell layers is of importance, as the stress development depends on the mutual relaxation of stresses due to creep. In the present study we focus on the creep of the anode and anode support of the SOFC as this, for anode supported cell designs, constitutes the main structural component, with the anode being 30 to 100 times thicker than the electrolyte. The anode is typically made from nickel (Ni) and 3 or 8 mol % yttria partially stabilized zirconia (3YSZ and 8YSZ, respectively) dependent on whether mechanical strength or ionic conductivity is of primary importance.

Gutierrez-Mora et al. [13] and Morales-Rodriguez et al. [14,15] measured the creep rate of Ni-3YSZ and Ni-8YSZ anodes, respectively, in compression at high temperatures, i.e. ~1000-1200°C. Gutierrez-Mora et al. came to the conclusion that Ni was determining the creep rates at these temperatures, whereas Morales-Rodriguez came to the conclusion that 3YSZ determines the creep rate. The investigated temperatures are however in both cases somewhat higher than the temperature range currently considered for SOFC operation (~700-850°C).

Laurencin et al. [16] measured the creep of Ni-8YSZ in bending at 700-850°C. From an analytic microstructural model they found that the creep of the cermet to a large extent is determined by the creep of the 8YSZ in this temperature range, as the measured Ni-8YSZ and the modeled creep of 8YSZ were relatively close. They also investigated the ratio between layers, which are plane strain or plane stress conditions in beams during creep testing. They showed that the stress field was

mainly governed by plane stress conditions, even for a relatively wide beam (width / thickness = 7). Finally, they also showed that the creep was so fast under a simulated stack operation that after about 500 h the stresses would be halved under a typical operating condition [16].

Kwok et al. [17] studied the creep of Ni-3YSZ and Ni-8YSZ composites by a finite element micromechanical model of a reconstructed microstructure obtained using a focused ion beam together with a scanning electron microscope (FIB-SEM). The modeling results showed that the creep rates of both of the Ni-YSZ composites were identical to that of the porous YSZ backbones alone, and Ni could effectively be disregarded, when secondary creep is considered. The model also showed that the Ni phase was effectively unloaded within seconds even with the "slower" secondary creep.

Jiménez-Melendo and Huamán-Mamani [18] studied the creep rates under different atmospheres of NiO-3YSZ and NiO-8YSZ at 1200-1350°C. They found that the creep of the 3YSZ provided a higher ductility than the 8YSZ. This was due to the small grain size (0.4 μm) of the former composite, which allowed for superplastic behavior. Superplastic behavior has been studied widely [19], in particular for 3YSZ, 4YSZ and 8YSZ [20-23]. This is an important phenomenon but only relevant to temperatures much above preferred stack operation temperatures today.

In this work we report on a newly discovered creep phenomenon, which yields a deformation rate during reduction of NiO to Ni of a NiO-3YSZ anode support, which is much higher (~ $\times 10^4$) than the creep rate during operation with the anode-support in fully reduced state. This phenomenon will thus relax all the stress in the cell within minutes of the reduction process. This creep phenomenon occurs under combined loading and reduction. Thus, the effect of different combinations of onsets of load and reduction has been studied. Also the effect of mode of loading was studied by three-point bending experiments and uniaxial tension experiments. To explain the difference between the

creep rates observed under the two types of loading, further qualitative experiments showing the influence of stress on the nucleation of the reduction process (NiO to Ni) were conducted. For further elucidation of the phenomenon, the deformation during the reduction process was measured on anode supports in unloaded condition. Based on the different experiments, a hypothesis for explaining the observations was conclusively deduced.

2. Experimental

2.1 Materials and sample preparation

Two types of samples were prepared from anode supports of nickel-oxide (NiO) and 3YSZ in equal volumetric amounts. The first type of samples consisted of tape-cast and sintered anode supports. The thickness after sintering was 300-340 μm. A more detailed description of the fabrication procedure of anode supports can be found elsewhere [24]. The resulting microstructures have been studied previously [44-47].

As stated in [42] the characteristic time for diffusion through these anode supports is in the order of 50 ms, which is orders of magnitude faster than the reduction rates studied in this work, and is not significantly hindered by the presence of an electrolyte. Thus, the electrolyte can only influence the reduction process by acting as a mechanical constraint or external mechanical loading, and this influence must be indirectly estimated. Therefore, single layered Ni(O)-3YSZ anode supports are studied under controlled external loading for a clear interpretation of the results.

The second type of samples was manufactured by stacking and hot pressing (200 kN over 25 mm × 9 mm tapes for 1 min) of several layers of the above mentioned tapes (after tape-casting, before

debinding and sintering) followed by cutting and sintering to a dimension of 20 mm × 6 mm × 1 mm. Good adherence between the layers was achieved by this approach, and no cracks were found in the polished cross-sections investigated by scanning electron microscopy after the mechanical and chemical exposure (described further below).

The samples for the mechanical testing were made from the first type of samples by cutting to 15 mm × 60 mm and 2-5 mm × 20 mm after sintering for three-point bending and uniaxial tension, respectively. The porosity was measured by mercury porosimetry to be 17.0 % before reduction, and 39.4 % after reduction at 800°C.

A sample of "pure" 3YSZ was made from a sintered NiO-3YSZ sample, which was consequently reduced in 9% H_2 and 91% N_2 ('9% H_2' in the following) to Ni-3YSZ. The Ni was then leached out by submerging the sample into a stirred 4.5 M HNO_3 aqueous solution for four hours.

2.2 Experiments

2.2.1 Three point bending

The first experiment conducted was creep testing in three-point bending under constant load and with a shift of atmosphere from air to 9% H_2 at 800°C. The testing was performed in an in-house constructed setup based on a modification of the high temperature four point bending setup described in Ref. [7]. A hanging weight is used to apply a constant force on the sample. The fixture is located in a furnace with a controlled temperature and atmosphere. The beam span is 50 mm and the sample is centrally loaded. The setup allows direct view on the center of the sample and thus optical detection of its deflection with load over time. For details on the furnace, atmosphere control and the optical deflection detection technique please see Ref. [7].

2.2.2 Uniaxial tension

The uniaxial creep experiments are conducted in a thermo-mechanical analyzer (Netzsch, TMA 402 F1 Hyperion), which allows for individual control of loading and reduction. For the experiments the standard uniaxial fixture provided with the equipment was used. In this, the sample is fixed at both ends between two slabs of alumina, with an alumina screw going through the two slabs (see Figure 2a). A special device with rails is used to align the slabs and the sample during the fixation. Holes in the slabs allow for inserting a pin and hereby fixating the sample to the actuator in the Netzsch TMA. Various sequences of uniaxial loading and shift of atmosphere from air to 9% H_2 at 800°C were conducted. The distance between the grips, and thus the gauged length of the sample is 15 mm.

2.2.3 Three point bending and quenching

The three-point bending fixture can also be attached to an actuator, which can move the entire fixture up and down, see Ref. [7]. This enables movement of the fixture and the samples out of the hot part of the furnace, and thereby quenching of them. Thus, it is possible to follow the reduction process by ‘freezing’ it at different stages. The reduction process is however fast, and the best experimental results of this type, presented here, were obtained at 650°C. Two types of quenching experiments were conducted: three-point bending and single point compression. The three-point bending experiments are as described above, however with the fixture mounted on an actuator, which allows for quenching by fast movement into a cold zone in the furnace.

2.2.4 Single point compression and quenching

The single point compression experiment was carried out by compressing one end of the 1 mm thick sample in a fixture functioning as a screw clamp with a stainless steel screw. This was also mounted on the above-mentioned actuator to allow fast quenching. The purpose of this experiment is to observe the influence of stress on the reduction front in an experiment different from the three-point bending experiment. If any inter-laminar cracks were present from the processing this should not influence the reduction front significantly, as this propagates in parallel with crack orientation.

The actual stress level is challenging to measure in this experiment, as the contacting of the screw clamp on the microstructural scale will initially only lie on a few grains of the NiO-YSZ sample. However, with the firm tightening of the screw it can be assumed that the few initial contact points provoke local yielding of the steel, as compressive failure of the ceramic component will require very large stresses. This will lead to establishment of more contacting points. Thus, the highest stress level can be expected to be in the vicinity of the yield stress of the screw material (~300 MPa), depending on the geometry of the anode support microstructure.

2.2.5 Microscopy

The microstructure and chemical composition of the 1 mm thick compressed sample was characterized with a scanning electron microscope (SEM, Hitachi TM3000) equipped with backscattered electron (BSE) detector and an energy dispersive X-ray spectroscopy (EDS) SDD detector (Bruker Quantax 70) and operated at 15 kV. Sections of the samples were embedded in epoxy resin, polished and covered with a nanometer thin carbon layer. Standardless EDS analysis was performed using the Bruker Quantax 70 software to determine the local chemical composition of the sample.

3. Analysis

Creep is time dependent deformation of materials under load, and is typically split into three time domains; *Primary creep* with a high initial deformation rate, which due to hardening processes decreases to the steady deformation rate of *secondary creep*. During *tertiary creep* the material deteriorates and the creep rate increases towards failure [25].

Generally secondary creep for ceramics can be described by the empirical Norton Power Law [26]

$$\dot{\varepsilon} = \frac{1}{E_c}\sigma^n = \frac{ADGb}{kT}\left(\frac{b}{d}\right)^p\left(\frac{\sigma}{G}\right)^n, \qquad \text{where} \qquad \frac{1}{E_c} = \frac{ADb}{kTG^{n-1}}\left(\frac{b}{d}\right)^p. \tag{1}$$

Here, D is the diffusion coefficient of the relevant creep mechanism, G is the shear modulus, b is the Burger's vector length, k is Boltzmann's constant, T is the absolute temperature, d is the grain size, p is a size exponent, n is the stress exponent, and A is a dimensionless constant. To avoid un-physical results (complex numbers) Eq. (1) could more correctly be written:

$$\dot{\varepsilon} = \frac{1}{E_c}\operatorname{sgn}(\sigma)|\sigma|^n \tag{2}$$

To characterize the creep of ceramic materials both tensile and compressive uniaxial methods [14,27], biaxial bending methods [28] and uniaxial bending methods [29] have been used. In order to apply the beam bending methods, the stress distribution must be deduced by a combination of beam theory and the Norton Power Law, see Appendix A and Refs. [16,30].

3.1 Norton Power Law Creep parameters from three-point bending

In a beam the Bernoulli assumption (assumption of linear strain distribution over the cross section) can be applied with a good approximation, i.e. $\varepsilon = -\kappa y$, where κ is the curvature and *y* the vertical coordinate with origin at the bending center of the beam. The strain rate can thus also be expressed as

$$\dot{\varepsilon} = -\dot{\kappa} y \tag{3}$$

where $\dot{\kappa}$ is the rate of the curvature change ('curvature rate' in the following).

The stress distribution over the cross section can be obtained by combining Eqs. (2) and (3). The bending moment equivalent to these stresses can be obtained by integration, and hereby link the curvature rate and the bending moment, *M*, (see Appendix A)

$$\dot{\kappa} = \mathrm{sgn}(M)\left(\frac{|M|}{I_c}\right)^n \frac{1}{E_c} \tag{4}$$

where I_c is a "complex" moment of inertia, see Appendix A and Ref. [16].

The displacement rate, $\dot{v}^{\max}$, of the center of the beam can be obtained by integrating the curvature rate twice over the length, *L*, of the beam and applying the boundary conditions of three-point bending to obtain the unknown integration constants (see Appendix B)

$$\dot{v}^{\max} = \frac{\mathrm{sgn}(F)}{n+2}\left(\frac{|F|}{2I_c}\right)^n \frac{1}{E_c}\left(\frac{L}{2}\right)^{n+2} \tag{5}$$

where *F* is the loading force on the beam. Taking the logarithm to Eq. (5) and rearranging leads to

$$\log\left(\left|\dot{v}^{\max}\right|\right) = n\log\left(\left|F\right|\right) + \log\left(\frac{1}{n+2}\frac{1}{2^n E_c {I_c}^n}\left(\frac{L}{2}\right)^{n+2}\right) \tag{6}$$

Thus, the power, *n*, can be obtained as the slope of a linear fit of the logarithm of the displacement rate, $\dot{v}_j^{\max}$, to the the logarithm of the load, *F*. E_c can be deduced from the intersection with the *y*-axis, p_2, of the linear fit ($y=p_1x+p_2$) plotting $\log\left(\left|\dot{v}^{\max}\right|\right)$ versus $\log\left(\left|F\right|\right)$

$$E_c = \frac{1}{\exp(p_2)}\frac{1}{n+2}\frac{1}{2^n {I_c}^n}\left(\frac{L}{2}\right)^{n+2} \tag{7}$$

4. Results

4.1 Three-point bending experiments

The displacement due to creep of anode supports exposed to a constant load in three-point bending during a shift of atmosphere from air to 9%H_2 at 800°C is shown in Figure 1a for different load levels. The very large displacement shown as a vertical drop in all of the curves shown in Figure 1a, is what here is referred to as *accelerated creep*. After the fast initial creep occurring during the first ~10 minutes after the gas change, a slower creep rate is observed, which is the process normally characterized in creep measurements (labeled “normal creep” in Figure 1a). The displacement rate and thus also the directly deduced creep rate is *strongly* accelerated (~×10^4) at the shift of the atmosphere. The ‘steps’ on the normal creep part of the curves is a result of the large displacements from the accelerated creep, which causes the sample to slide over the support-pins and stop because of friction, in turn. That the amount of creep occurring during the reduction process is significant is

illustrated in the insert in Figure 1a, which shows a specimen mainly distorted by “accelerated creep”.

The deflection of the sample center point during the reduction is shown in greater detail in Figure 1b, where a clear load dependency can be seen. Applying the procedure discussed in Section 3, the power, *n*, in the Norton Power Law is determined by linear regression fitting of the logarithm of the creep rate versus the logarithm of the applied load, according to Eq. (6). The power *n* is determined to be ~0.8 for the accelerated creep regime and 1.9 for the normal creep regime in the fully reduced state. This indicates that both creep mechanisms are dominated by diffusional creep [25], although different.

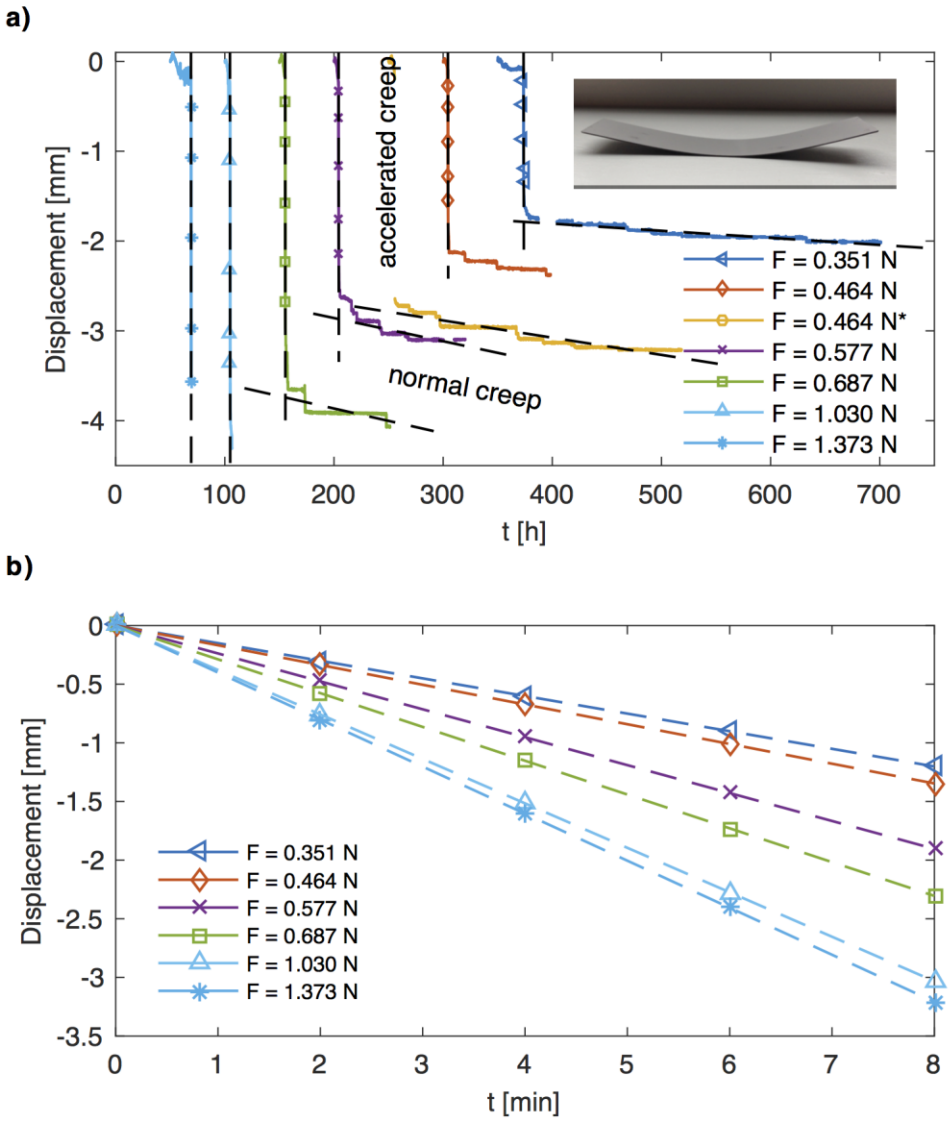

Figure 1 a) Displacement of the center of beams exposed to different loads in three-point bending and a shift of atmosphere from air to 9%H_2 at 800°C (resulting in accelerated creep). A close up on the steep decent during accelerated creep (marked with x's) are in b). The insert in a) shows the curvature of a sample after creep testing.

In the literature several studies of the volume change occurring during the reduction of NiO-YSZ structures have been reported, and a good overview can be found in the review in Ref. [6]. The reduction strain due to the transition of the NiO-YSZ structure to Ni-YSZ has been found to be about 0.01 % contraction by use of a contact dilatometer [6]. The observed bending cannot be explained as a superposition of this reduction volumetric change, as the reduction contraction would in the end be equal over the entire cross section and thus not give rise to any bending. Unless the contractions from reduction occur at different locations over time in the sample and are combined with time dependent processes as creep.

4.2 Uniaxial tension experiments

To exclude that the accelerated bending rate is due to e.g. an asymmetric reduction profile and thus also asymmetric internal stresses and creep rates, uniaxial tension experiments were also conducted.

The accelerated creep occurs only when both load and reducing atmosphere are present. In Figure 2a the creep response to different combinations of uniaxial load and gas shift to reducing atmosphere are explored. t=0 corresponds to a situation, where the sample suddenly experiences load *and* reducing atmosphere. Sample 5 is however tested in air (as a reference). Table 1 provides an overview of the samples loaded with 2 MPa at 800°C in uniaxial tension.

The accelerated creep rate is shown to depend on the load level (Figure 2b); it increases for increasing loads, as expected. The increase in strain is however not linear with stress and does not depend on the stress with the power of 0.8 (as in the three-point bending experiments), as more than a doubling of the stress level does not result in the double amount of creep.

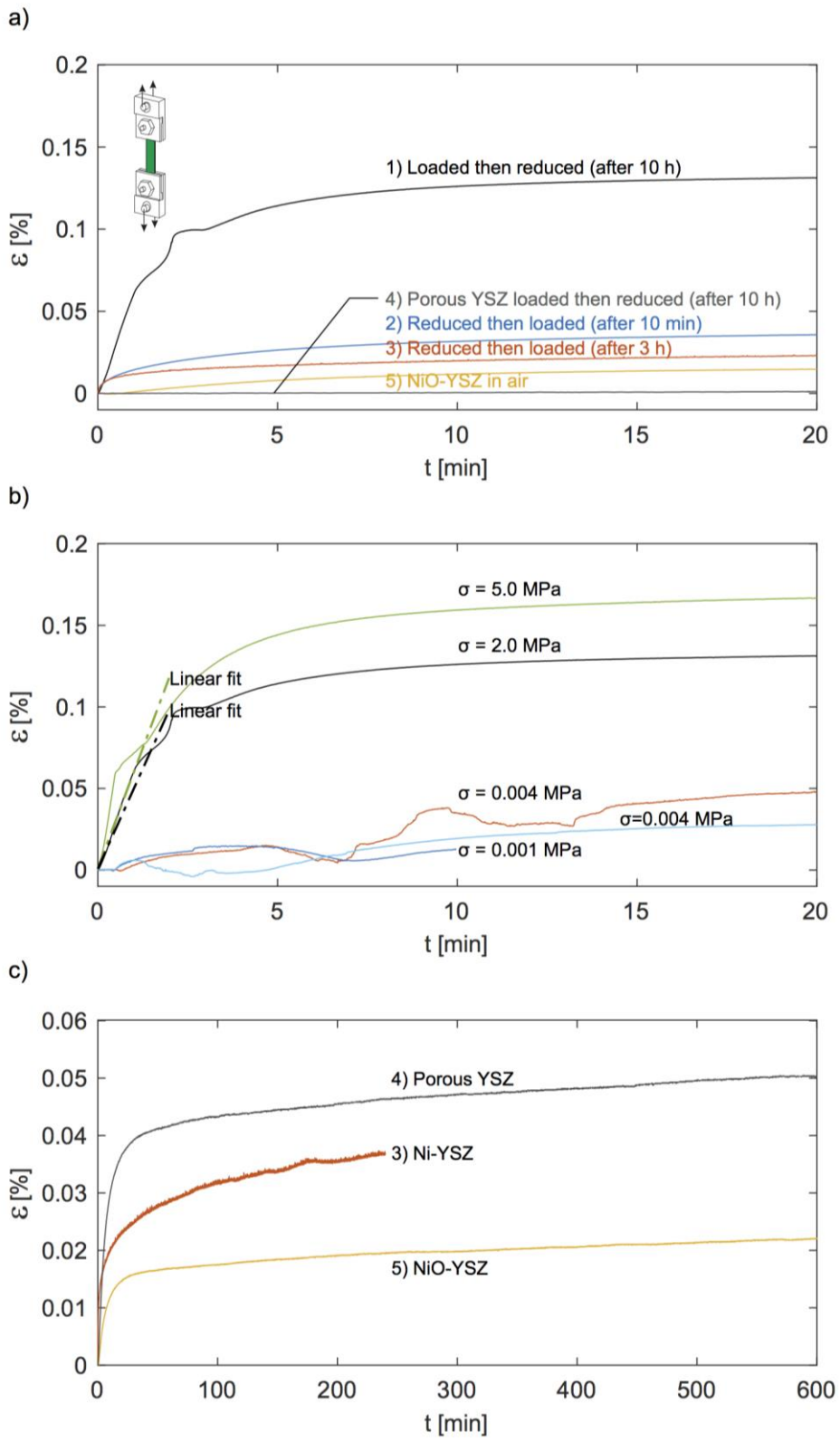

Figure 2 Creep strain over time for different initiations of uniaxial loading. a) For different initiations of

uniaxial loading relative to the initiation of the reduction (red.) at 2 MPa of load. Please refer to the Table 1 for a detailed explanation of the curves plotted. The insert illustrates the fixture used for the experiments. b) For different load levels with two linear fits to the first 50 s of the two creep curves for 2 and 5 MPa of creep. c) For NiO-YSZ, Ni-YSZ and pure YSZ with the Ni phase leached away, including primary creep and no change of atmosphere.

To quantify the creep rate of the accelerated creep in uniaxial tension, the secondary creep law (Eq. (2)) has been fitted to the initial creep response assuming that n equals 0.8 as in the three-point bending experiments (see the linear fits in Figure 2b). Comparing the resulting E_c values to those from three-point bending, the uniaxial creep rates are seen to be significantly faster, i.e. 45 and 72 times faster, see Table 2. The reduction kinetics might explain these deviations as discussed in the next section.

Also, as seen in Figure 2b, an expansion is observed during the reduction at almost zero load (~0.001 MPa) in uniaxial tension (more observations were recorded than those shown in the graph). This is different from previous measurements, as a contraction due to the reduction has generally been observed in the literature [6].

In Figure 2c the primary creep and part of the secondary creep for the different material compositions is plotted over the first 10 hours of creep for cases with no change of atmosphere. The slope of the secondary creep curves (of sample 3 and 4), here taken from 150 min to 600 min of creep, are fitted with Eq. (2), and the results are summarized in Table 2.

4.3 Stress dependent reduction

Simonsen et. al. showed by *in situ* reduction of a NiO-YSZ cermet in an environmental transmission electron microscope that the reduction is nucleated at some point in the nickel oxide phase and spreads from there [31]. Thus, different parts of the sample are exposed to accelerated creep at different points in time. Wider samples will therefore not experience the accelerated creep over the entire cross section at the same time, as the reduction needs to spread. This would explain the slower creep in the wider three-point bending sample (~15 mm compared to 2-5 mm wide uniaxial tension samples). Furthermore, another effect might slow down the creep in the three-point bending, i.e. a stress promoted nucleation of the reduction. This phenomenon will be described in the following.

Our hypothesis is that the reduction in a stressed anode support is promoted by stress, i.e. the points with the largest stress reduces firstFapp. That chemical processes are influenced by stress (chemo-mechanical coupling) is well known, see e.g. [32]. The elastic energy of a NiO particle in compression will be released on reduction due to the volume change and the redistribution of the material. The elastic energy adds to the free energy and thus acts as an additional “driving force” for the reduction on top of the chemical one. This is further verified by the experiments presented below, where the samples are quenched during the reduction process.

Figure 3a shows the top and bottom of three samples all quenched from 650°C, 60 seconds after change of inlet gas composition, where sample I was loaded with 2.44 N in three-point bending, and sample II and III were unloaded reference samples located adjacent and above it (slightly warmer 2-3°C), respectively. The samples presented in Figure 3 are predominantly green, which means that the reduction process was interrupted at a very early stage (approximately 60 seconds after change

of inlet gas). It is clear that sample I contains more reduced phase (gray colored areas) than the reference sample II (which is still predominantly green). Moreover, sample I is gray (reduced) predominantly in the area where the highest compressive stress occurred, i.e. in the center of the top of the sample. This indicates that stress, and in particular compression, can accelerate and thus nucleate reduction of NiO in anode supports. The progression of the reduction in sample III shows that the reduction rate is highly sensitive to temperature.

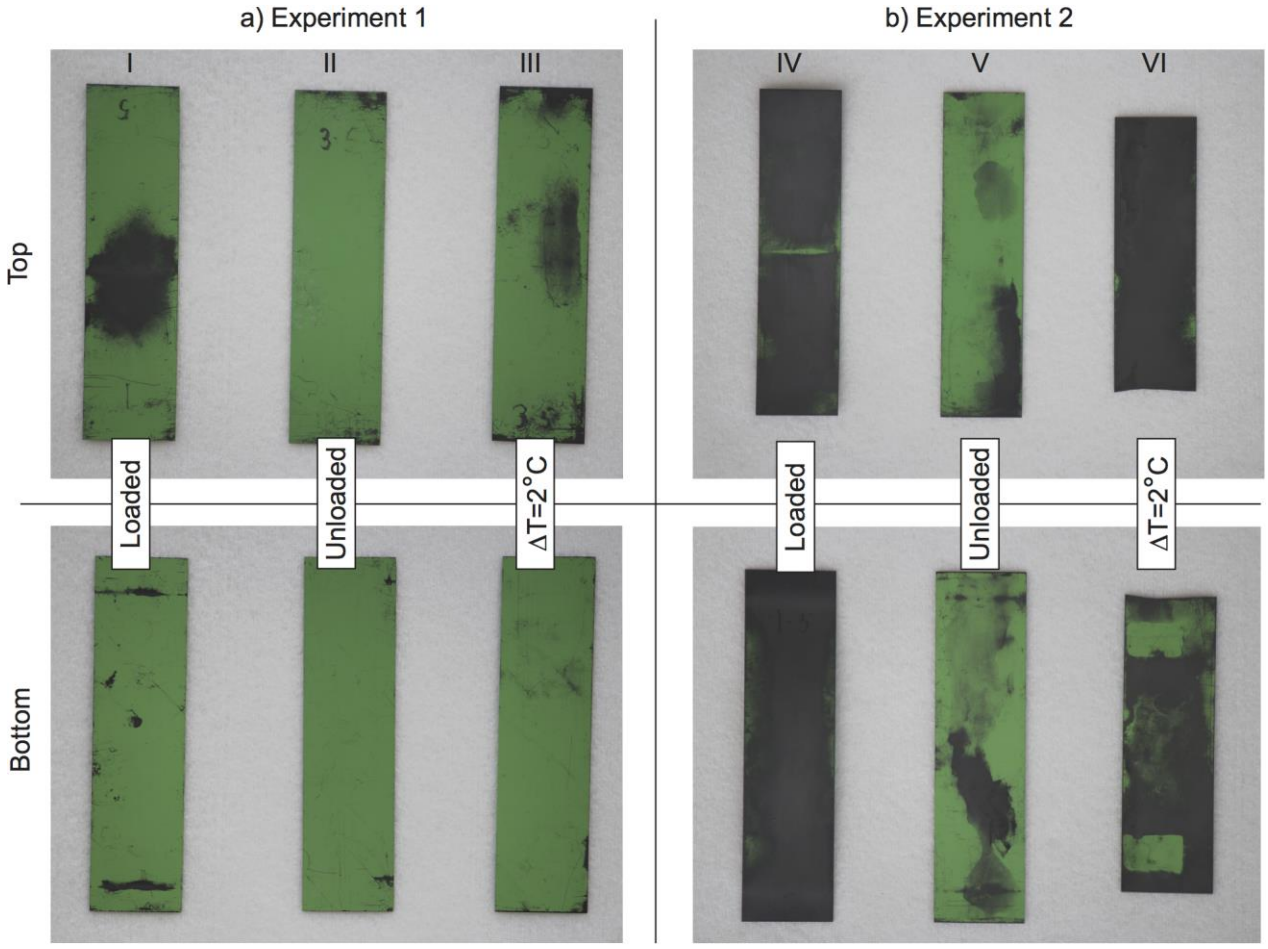

Figure 3 Pictures of top and bottom of two samples quenched from 650°C 60 seconds after change of inlet gas composition. Sample a) has been exposed to three-point bending with 2.44 N of load, b) an unloaded reference sample at same location in the furnace, c) an unloaded reference sample at a warmer location in the furnace (2-3°C).

Figure 3b shows an analogous set of samples at a more advanced reduction stage although the two sets of samples experienced the same measurable reduction conditions, i.e. 650°C, 2.44 N of load (samples I and IV) and 60 seconds of 9 % H_2 exposure before quenching. The difference in exposure stems from small variations in temperature, gas switching time and gas compositions, which are not measureable. Again it is clear that the stressed sample (IV) reduces faster than the reference sample (V).

To exclude that it is the lower side of the sample, which reduces faster because of the gas flow direction in the furnace [7] the anode support was also tested with a single point in compression (achieved by a screw clamp). In Figure 4 the quenched single point compressed sample is seen. Again the result implies that the high stress has promoted the nucleation of the reduction. This confirms that stress is the nucleating factor and not e.g. asymmetric exposure of the sample because of e.g. gas flow directions etc.

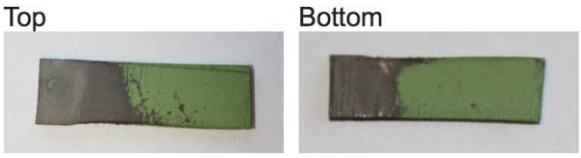

Figure 4 Top and bottom of single side compressed sample, where the left side was exposed to the compression.

In Figure 5 SEM images of the cross sections of the single point compressed sample are shown. Image a) presents cross section of the sample close to the right end of the sample (green end), and image b) – close to the left (gray) end. The porosity of the material in the image b) is evidently larger than in image a), which shows a higher degree of reduction (as NiO takes up more volume than Ni). This is confirmed by the EDS measurement, which shows that the percentage of oxygen

for the area presented in image a) was about 28 weight % and for the area in image b) only about weight 16%.

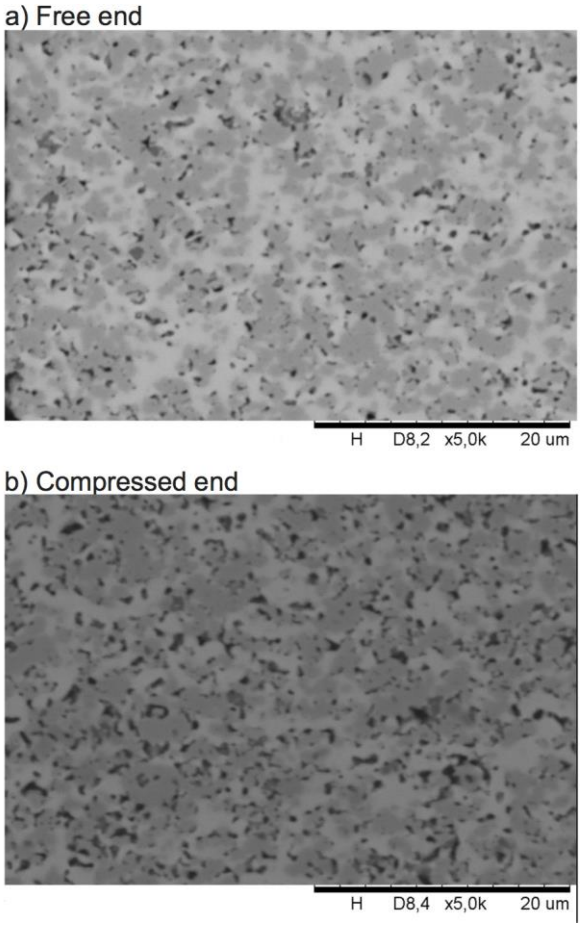

Figure 5 SEM images for cross sections of the single point compressed sample at a) free end (28% oxygen), b) at compressed end (16% oxygen).

Thus, this phenomenon could explain the different creep rates determined in the three-point bending experiment and the uniaxial tension experiment, as it is only a part of the samples in three-point bending, which experiences the accelerated creep, and the total deformation rate is therefore slower. This also means that the stress analysis in section 3 should be revised, as this analysis assumes isotropic material properties over the cross section of the beams. The purpose of the analysis is however to show that the deformation rates recorded in theses experiments are orders of magnitude

larger than those recorded in other creep experiments [16]. A revised analysis would also involve the reduction rate and a more detailed material model of the three interacting phases including primary and secondary creep for all phases (NiO, Ni, YSZ). It is beyond the scope of this work to make such an analysis.

The stress-induced reduction is currently being studied further by energy-resolved neutron imaging [33,43]. Among others, the objective is to study the progress of the reduction process in-situ by following the Bragg edges of NiO and Ni across similarly stressed anode support samples.

4.4 Rate of density change during reduction

To investigate how the accelerated creep process relates to the reduction process, samples in the three-point bending experiment were quenched after different periods of reduction exposure at 650°C. The weights of the samples were measured before and after the quenching. From this the relative change of mass for different reduction periods were deduced, see Figure 6.

The relative change of mass is seen to follow an exponential trend with time, t

$$\Delta m = \Delta m_{\infty}\left(1-\exp\left(-\frac{t}{\tau}\right)\right) \tag{8}$$

where Δm_{∞} is the change of mass for a full reduction, and τ is the characteristic time of the reaction, which depends on temperature through an Arrhenius type expression

$$t = \frac{t_0}{\exp\left(-\frac{E_a}{RT}\right)} = t_0 \exp\left(\frac{E_a}{RT}\right) \tag{9}$$

where R is the universal gas-constant, T the temperature in Kelvin, t_0 is a constant, and E_a the activation energy. The E_a has experimentally been determined to be 68 kJ/mol [40].

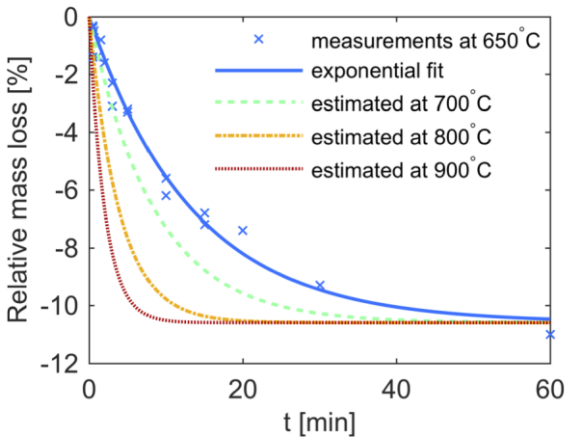

Figure 6 Relative mass loss of samples quenched from 800°C after different periods of reduction together with an exponential fit of the measurements. The estimates of the kinetics at 700°C, 800°C and 900°C are based on the exponential fit and an activation energy of 68 kJ/mol [40] as described in the text.

The relative change of mass Δm_∞ can be calculated from the composition of the anode support to be 10.7 %, and by the curve fitting this factor is determined to be 10.6 %. The pre-exponential constant t_0 is determined to be $1.91 \cdot 10^{-3}$ s, providing characteristic reaction times, τ, of 13 minutes and 4 minutes at 650°C and 800°C, respectively (the latter matching the characteristic time of the accelerated creep response at 800°C). The estimated reaction kinetics at different relevant temperatures is shown in Figure 6.

5. Discussion

By considering Figure 1, 2 and 6 it is clear that the large deformations observed occur because of the reduction and within the same time interval as the reduction, and the phenomena are therefore

inherently connected. This has also been confirmed recently in-situ neutron imaging of the deflection and material phases of a loaded anode support during reduction [43]. A hypothesis to explain the magnitude of the observed deformations is outlined in the following.

5.1 Explanation for expansion during reduction in unloaded condition

The observed expansion during reduction in a practically unloaded condition shown in Figure 2c (three lower curves) is opposed to other literature, (see overview in Ref. [6]), where unloaded samples have been observed to contract during reduction in a contact dilatometer, where a compressive load is applied to the sample. The previous explanation for the measured contraction of the anode supports during reduction relates to the significant volumetric ratio (Pilling-Bedworth ratio) between NiO and Ni (approximately 1.65:1). Thus, the explanation was that the large contraction of one of the phases would lead to an average contraction of the composite during the reduction.

The influence of this contraction on the composite anode does however depend on the balance between the stiffness of the two phases (Ni and YSZ) during the reduction, where the stiffness relates to the material properties, composition, and microstructure. Ni phase creeps very fast compared to the YSZ backbone [34], and thus it is quite soft compared to the YSZ phase. Also during the reduction NiO reacts to form Ni and the high mobility of the cations in this period makes it reasonable to assume that the compliance of the material is very high during this period. Thus, given similar contiguity and volumetric ratio, the YSZ phase will determine the macroscopic behavior of the composite.

Furthermore, internally in the Ni-YSZ microstructure residual stresses must be present, as the thermal contractions from the sintering temperature of the two phases are different. The thermal expansion coefficient of YSZ is lower (~$11 \cdot 10^{-6}$ K^{-1}) than that of NiO (~$14 \cdot 10^{-6}$ K^{-1}) [35], which means that compressive stresses builds up in zirconia while cooling from sintering temperature to operation temperature or room temperature [36].

Hence, we believe that the expansion that all these mildly loaded samples experience on reduction is due to a release of the internal compressive residual stress in the YSZ phase with the softening of the Ni as illustrated in Figure 7a-c. Onwards this strain will be referred to as reduction strain.

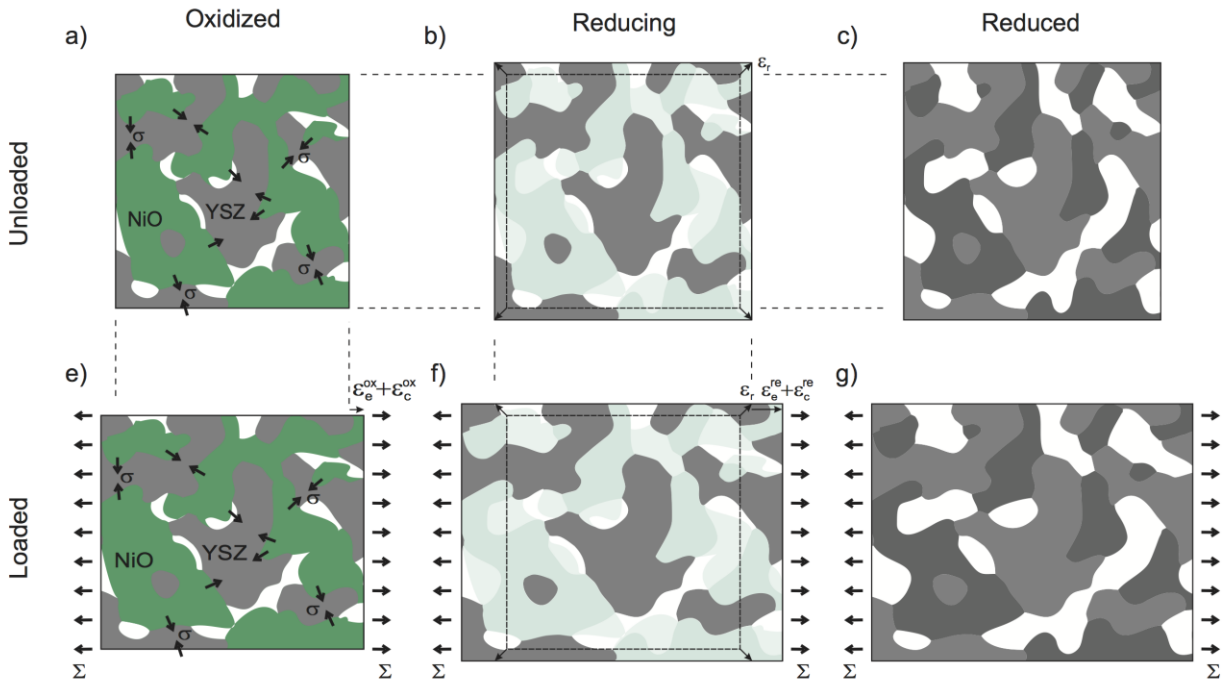

Figure 7 Schematic representation of the deformations occurring during reduction in unloaded condition due to internal residual stresses, σ (sub figures a-c), and in loaded condition due to a combination of internal residual stresses, σ, and stresses from external loads, Σ (sub figures d-f). During the reduction (sub figures b and e) the Ni can be assumed to be very compliant and not present any resistance to the external load.

From the reduction strain it is also possible to estimate the unknown micro-strain in the YSZ phase before the reduction. With an expansions of 0.04-0.05 % as measured here, the average local residual compressive stress in the YSZ phase can be deduced to be in the order of 60-80 MPa at 800°C before reduction, given a Young's modulus of 157 GPa [4]. This corresponds to an equivalent stress (traction on the surfaces of a unit cell including pores) of 6-8 MPa, as the correction factor on the Young's modulus for 59 % of porosity is 0.10, i.e. the Young's modulus of the porous YSZ structure is 15.7 GPa (obtained by elastic simulation of the same microstructure as in Ref. [34]).

5.2 Explanation for the deformations during reduction in loaded condition

For the uniaxially loaded samples, the reduction strain explains the 0.04 to 0.05 % of the total strain of 0.12 % through the accelerated creep phase (see Figure 2b). Under the assumption of zero resistance of the Ni phase during reduction, the primary creep of the YSZ will contribute with 0.04 % of strain (see Figure 2c). The final amount of strain arises from a significant change of elastic modulus going from NiO-YSZ (181 GPa [37]) to a porous YSZ structure with 59 % of porosity (15.7 GPa [38]) given zero resistance to deformation of the Ni phase (see Figure 7d-f). Onwards this will be referred to as the elastic contribution. The difference in elastic strain from this is thus ~0.01 % (2 MPa·(1/15.7 GPa – 1/181 GPa)). Summing these three contributions (0.09 % to 0.10 % in total) almost provides the total measured strain during the reduction (0.12 %).

In the samples loaded in bending the expansion from the reduction expansion occurs equally over the entire cross section, and hence will not contribute to the deflection. This might also partly explain why the recorded deformations during reduction in the uniaxial tension experiment are

faster than in the bending experiment, since in the uniaxial case the reduction strains contribute to the elongation.

In Figure 8 the maximum measured strains occurring in the bended beams (at the center of the bottom) are compared to calculated strains due to the elastic contribution (change of Young's modulus). In this case the difference between the total strain and the elastic contribution can be assumed to be due to primary creep of the porous YSZ. The contribution from the primary creep is thus approximately 1/3 of the total strain (see Figure 8). In the uniaxial loading case the primary creep contributes with 4/5 (0.04 % / (0.04+0.01 %)) of the total strain, when the residual stress release is disregarded (for comparison). Again the uneven reduction of the specimen in bending might explain why the primary creep do not contribute as much; the creep deformation is restrained from the surrounding oxidized material, which is why the entire sample does not yield at the same rate as the uniaxially loaded sample. In the final measurement (F = 1.03 N, ε=0.35 %) the sample broke during the accelerated creep. This is in good correspondence with the measurement of failure strain of 0.38 % of 3YSZ at 800°C reported in ref. [37].

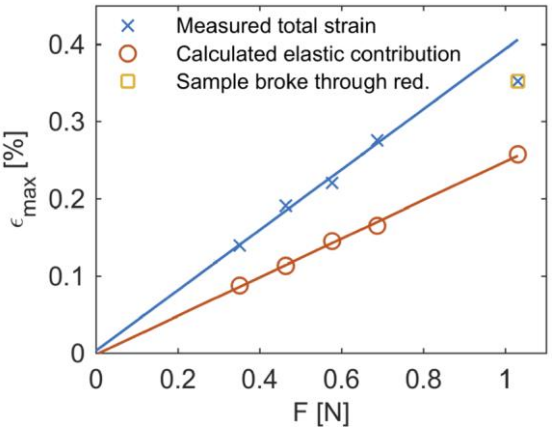

Figure 8 The maximum strain in the beams from the bending during reduction compared to the maximum change of strain due to the change of elastic modulus from that of NiO-YSZ to porous YSZ during reduction.

The measurement marked with a square marks the maximum strain recorded in the experiment before the sample broke.

If the recorded strains in the YSZ phase in the bending experiments are elastic to a high extend while being bended (~2/3), the unconstrained strongly deformed sample (see insert in Figure 1a) at room temperature deserves further explanation. The reason for this deformation is that the Ni is deformed by fast creep and reshaped during reduction (Figure 7e), while a constant load is kept on the sample until it reaches room temperature. During cooling to room temperature the Ni will consolidate and "freeze" the shape of the sample (Figure 7f). This also means that the internal stresses in the YSZ phase balance the external load completely until the consolidation occurs (including redistribution and coarsening). The sample must at room temperature thus have residual stresses in the YSZ phase, which vary linearly over the thickness of the beam (compressive in the top and tensile in the bottom). These residual stresses will be superimposed with stresses due to the difference in thermal contractions of the two phases from the consolidation temperature, which is now the new so-called reference temperature for residual stresses. When the load is removed the sample would partly bend back towards the original flat shape, but it is hindered by the Ni phase, which was situated in an unstressed condition after the reduction (before the cooling).

Hence, in general most of the observations recorded in this work can be explained by assuming that Ni is creeping very fast during the reduction, i.e. the stresses in NiO are completely relaxed such that the Ni phase is free of stress just after reduction. The YSZ phase of the composite structure does therefore carry the entire load, which leads to both a significant amount of primary creep of the YSZ phase alone and a significant change of elastic modulus of the sample (resulting in a change in elastic deformation). The authors also considered micro-cracking of the YSZ in tension as an apparent softening mechanism, but did not observe any micro-cracks. As many cells are curved

before the point of reduction (due to thermal expansion mismatches of the different layers), and are therefore exposed to similar loads and reduction as in this study, this would also imply that micro-cracks should be broadly observed upon reduction of cells, and this is not the case.

The differences in the apparent creep rate between the uniaxially tensed samples and bended samples might be explained by the demonstrated stress promoted reduction nucleation phenomenon, which further leads to the above-mentioned hindrance of localized primary creep in the asymmetric reduction during bending. This difference between bending and uniaxial loading does however deserve more research.

5.3 Consequences of the accelerated creep

The accelerated creep has been observed both in three-point bending (section 4.1) and in uniaxial tension (section 4.2) for different load levels and has been shown to be orders of magnitude faster than the 'normal creep' occurring during operation of the SOFC. Stresses are thus relaxed very fast in a multilayered SOFC structure during reduction. Depending on the sealing procedure and fixation of the cell in a SOFC stack the stresses in the SOFC will change significantly during the reduction procedure. Based on the observations in this work the consequences of the accelerated creep are that:

1. For an *unconstrained* NiO-YSZ anode the internal (micro) residual stresses residing between the phases should go to zero at the point of reduction. With the Ni quickly re-arranging by creep. The consequence is that the effective coefficient of thermal expansion (CTE) of the composite will depend on the rate of the temperature change at elevated temperatures. The reason for this is that with very slow temperature changes creep will relax the stresses built up in the Ni phase, and the CTE of the composite becomes that of YSZ.

Oppositely, at very fast cooling, creep will not occur, and the measured CTE will be a (elastic) stiffness weighted average of the CTE of the two phases. In the former case residual stresses will thus relax while approaching room temperature after reduction. This and relaxation of the residual stresses during reduction have been observed in another on-going work by some of the current authors. In this work the residual stresses were measured in-situ with X-ray diffraction [41].

2. For an *unconstrained* SOFC half-cell (no cathode) the (macro) residual stresses residing amongst the layers should also go to zero at the point of reduction, as all the layers can be considered to be pure (porous and solid) YSZ during the reduction. This is well in line with the study by Sun et. al. [39] who measured residual stresses in SOFC half-cells at room temperature. They reported that: *"the assumption of full plastic relaxation at the reduction temperature gives curvatures in much better agreement with the measurements (although slightly overestimated) and lower residual electrolyte stresses closer to the measured values (again slightly overestimated)."*, where they relate the residual stresses to the curvature of a free standing cell.

3. For an *unconstrained* full SOFC with cathode the macroscopic residual stress will of course also depend on the thicknesses, coefficients of thermal expansion (CTE), Young's moduli and the sintering temperature. In general, the cathodes are much thinner than the anodes, to avoid delamination of this layer, which typically has a higher CTE [6], and thus the residual stresses of the half-cell after reduction will still approach zero in this case. The amount of residual stress in the cathode after reduction will besides the dependence on the above mentioned parameters also depend on the primary creep of the YSZ phase and the elastic

contribution (from change of Young's modulus during reduction, see above). As the cathode sintering temperature is only moderately higher than the reduction temperature, it would in many cases be a reasonable approximation to assume *that the residual stresses in the cathode (and the entire cell) is zero at the point of reduction*.

4. For a *constrained* SOFC (e.g. a cell constrained by sealings and external loads on the SOFC stack) the external loads on the cell will be balanced completely by stresses in the YSZ structure (see above discussion in Section 5.2) during the reduction. The Ni will thus consolidate with zero stress on a strained YSZ skeleton. If the external loads were removed, the residual stresses in the YSZ induced by the external loads would now be balanced by opposing residual stresses in the Ni phase and thus be relaxed elastically (depending on the stiffness ratio between the Ni and YSZ microstructures). The residual protective compressive stress may thus also be preserved in the YSZ phase, if the seals are rigid (e.g. crystallized) and strong enough at the point of reduction. If a particular stack design has problems with durability of the seals, reduction of the SOFC stack should be considered immediately after sealing the stack, as the seals might at this point be ductile and compliant to release the compressive residual stresses in the YSZ phase (in electrolyte and anode). Doing so would also minimize the initial stress level of the sealings, as the expansion of the YSZ from release of internal residual stresses can occur, which is prevented when the sealings are crystallized.

In principle the observed phenomenon complicates a thermo-mechanical simulation of a SOFC stack considerably, as the phases of Ni-YSZ layers in principle must be considered individually. Especially because the failure of Ni-YSZ seems to be related to the straining of the YSZ phase rather than the average stress on the multiphase structure [37]. In many cases it is reasonable to

assume that all stress goes to zero in the SOFC stack at the point of reduction (see above discussion), which simplifies the thermo-mechanical analysis. This does however require an initial evaluation in each particular case.

6. Conclusions

In this work a newly discovered phenomenon, so-called accelerated creep, is presented. This occurs during simultaneous loading and reduction of solid oxide fuel cell NiO-3YSZ anode supports. The deformation rate during the accelerated creep has in this work been found to be several orders of magnitudes faster than during normal creep ($\times 10^4$). Thus, the accelerated creep rate is so significant that it has to be accounted for in construction of as well as analysis of the robustness of SOFC stacks, as all cells are at some point exposed to a reducing atmosphere under the mechanical constraint of the stack.

The creep during reduction was studied in various three-point bending experiments and in uniaxial tension experiments, where different combinations of load and reduction onset and chemical treatments were conducted to explore the phenomenon. Through this a hypothesis to explain the observations was given; that the Ni(O) phase creeps very fast during the reduction of the composite Ni(O)-YSZ structure, and that it therefore can be disregarded mechanically during the reduction. The consequence of this is that the fast deformations can be separated into three contributions: 1) expansion from reduction (relaxation of residual stresses), 2) primary creep of the YSZ skeleton and 3) an elastic contribution.

1) was observed in unloaded samples of NiO-YSZ, which is contrary to previous observations. The expansion can however be understood based on the above hypothesis, as the expansion is then a

release of internal (micro) residual compressive stresses in the YSZ at the softening of the NiO phase to Ni.

2) occurs with the softening of the NiO phase to Ni as the YSZ skeleton consequently carries all the load, which induces an extended amount of primary creep. This was also observed experimentally on a porous YSZ sample, which had been produced by leaching away Ni from a Ni-YSZ sample.

3) is also a consequence of the softening of the Ni phase during reduction, as the Young's modulus of the composite hereby changes significantly (from ~180 GPa to ~16 GPa), which results in additional elastic deformation.

The creep rate was found to differ in three-point bending and uniaxial tension. This is partially because the expansion during reduction does not contribute to the bending, as it occurs uniformly over the beams, but does contribute to elongation of the uniaxially tensed samples. Furthermore, a hypothesis of the influence of stress on the reduction rate (chemo-mechanical effect) influencing the deformation rates was also given. By experiments where anode support samples exposed to load during the reduction were quenched in the process, it was observed that the reduction is promoted at high stress locations, and that the reduction of the loaded samples is faster than in unloaded reference samples. This could explain the slower deformation of the larger three-point bending samples, as creep only occurs locally at the points with highest stress in contrast to the uniaxially (uniformly) stressed sample, where the creep would occur more or less simultaneously in the entire sample. Furthermore, it was speculated that the primary creep of the YSZ backbone was constrained by the surrounding slowly creeping unreduced NiO-YSZ.

The primary creep of a reduced anode support was measured to be significant (~0.01 % at 2 MPa after ~7 minutes of creep) also in reduced state after the accelerated creep, and thus this has to be taken into account in thermo-mechanical simulations of SOFC stacks as well as secondary creep.

The consequence of the observed phenomenon of accelerated creep was discussed at some length. In principle the thermo-mechanical analysis of a SOFC stack becomes more complicated with these findings, as the phases of the Ni-YSZ layers should be considered individually. As argued in the text it can however in many cases reasonably be assumed that all stress goes to zero in SOFC stacks at the point of reduction. Such assumption simplifies the thermo-mechanical simulations considerably. However, an initial evaluation for each case considering the influence of external constraints (external loads and interaction with the remaining stack) as well as internal balancing of stress with the cathode layer through the reduction is necessary.

A challenge for the thermo-mechanical modeling is however that the two different phases (Ni and YSZ) in principle should be considered independently in a more complex material model for the composite. This amongst others would lead to temperature rate dependent effective thermal expansion coefficients for the Ni-YSZ composites, due to the fast creep of the Ni phase.

Acknowledgements

The research leading to these results has received funding from the European Union's Seventh Framework Programme (FP7/2007-2013) for the Fuel Cells and Hydrogen Joint Technology Initiative under grant agreement n° 325278 and from Energinet.dk under the Public Service Obligation, ForskEL contract 2014-1-12236. The authors would also like to acknowledge John Johnson for his assistance with design of equipment and conduction of experiments.

References

[1] A. Selcuk, A. Atkinson, J Am Ceram Soc. 83 (2000) 2029-2035.

[2] M. Radovic, E. Lara-Curzio, Acta Mater. 52 (2004) 5747-5756.

[3] J. Laurencin, G. Delette, M. Dupeux, Journal of the European Ceramic Society. 28 (2008) 1-13.

[4] A. Atkinson, A. Selcuk, Solid State Ionics. 134 (2000) 59-66.

[5] J. Malzbender, R.W. Steinbrech, L. Singheiser, Advances in Solid Oxide Fuel Cells. 26 (2005) 293-298.

[6] A. Nakajo, J. Kuebler, A. Faes, U.F. Vogt, H.J. Schindler, L. Chiang, S. Modena, J. Van Herle, T. Hocker, Ceram.Int. 38 (2012) 3907-3927.

[7] H.L. Frandsen, D.J. Curran, S. Rasmussen, P.V. Hendriksen, J.Power Sources. 258 (2014) 195-203.

[8] G. Anandakumar, N. Li, A. Verma, P. Singh, J. Kim, J.Power Sources. 195 (2010) 6659-6670.

[9] A. Nakajo, F. Mueller, J. Brouwer, J. Van Herle, D. Favrat, Int J Hydrogen Energy. 37 (2012) 9249-9268.

[10] A. Nakajo, F. Mueller, J. Brouwer, J. Van Herle, D. Favrat, Int J Hydrogen Energy. 37 (2012) 9269-9286.

[11] F. Greco, H.L. Frandsen, A. Nakajo, M.F. Madsen, J. Van herle, Journal of the European Ceramic Society. (2014).

[12] A. Nakajo, P. Tanasini, S. Diethelm, J. Van Herle, D. Favrat, J.Electrochem.Soc. 158 (2011) B1102-B1118.

[13] F. Gutierrez-Mora, J.M. Ralph, J.L. Routbort, Solid State Ionics. 149 (2002) 177-184.

[14] A. Morales-Rodriguez, A. Bravo-Leon, A. Dominguez-Rodriguez, S. Lopez-Esteban, J.S. Moya, M. Jimenez-Melendo, Journal of the European Ceramic Society. 23 (2003) 2849-2856.

[15] A. Morales-Rodriguez, A. Bravo-Leon, A. Dominguez-Rodriguez, M. Jimenez-Melendo, J Am Ceram Soc. 91 (2008) 500-507.

[16] J. Laurencin, G. Delette, F. Usseglio-Viretta, S. Di Iorio, J.Eur.Ceram.Soc. 31 (2011) 1741-1752.

[17] K. Kwok, P.S. Jørgensen, H.L. Frandsen, J. Am. Ceram. Soc. (2015).

[18] M. Jimenez-Melendo, F.A. Huaman-Mamani, Solid State Ionics. 225 (2012) 471-475.

[19] T. G. Nieh, J. Wadsworth,O.D.Sherby, Superplasticity in Metals and Ceramics, Cambridge University Press, Cambridge, 1997.

[20] K. Kajihara, Y. Yoshizawa, T. Sakuma, Acta Metall.Mater. 43 (1995) 1235-1242.

[21] A. Bravoleon, M. JimenezMelendo, A. DominguezRodriguez, Scr.Mater. 35 (1996) 551-555.

[22] B. Kim, K. Hiraga, K. Morita, Y. Sakka, T. Yamada, Scr.Mater. 47 (2002) 775-779.

[23] A.A. Sharif, M.L. Mecartney, Journal of the European Ceramic Society. 24 (2004) 2041-2047.

[24] S. Ramousse, M. Menon, K. Brodersen, J. Knudsen, U. Rahbek, P.H. Larsen, Solid Oxide Fuel Cells 10 (Sofc-X), Pts 1 and 2. 7 (2007) 317-327.

[25] P. Paufler, Crystal Research and Technology. 21 (1986) 1338-1338.

[26] W.R. Cannon, T.G. Langdon, J.Mater.Sci. 18 (1983) 1-50.

[27] H.L. Lein, K. Wiik, M. Einarsrud, T. Grande, J Am Ceram Soc. 89 (2006) 2895-2898.

[28] F.L. Lowrie, R.D. Rawlings, B.C.H. Steele, W. Kleinlein, Proceedings of the Fourth International Symposium on Solid Oxide Fuel Cells (SOFC-IV). (1995) 318-325.

[29] A. Lakki, R. Herzog, M. Weller, H. Schubert, C. Reetz, O. Gorke, M. Kilo, G. Borchardt, Journal of the European Ceramic Society. 20 (2000) 285-296.

[30] A. Atkinson, J. Kim, R. Rudkin, S. Taub, X. Wang, J Am Ceram Soc. 94 (2011) 717-724.

[31] S.B. Simonsen, J.B. Wagner, T.W. Hansen, K. Agersted, K.V. Hansen, T. Jacobsen, L.T. Kuhn, (2013).

[32] H. Schmalzried, Solids in Thermodynamic Potential Gradients, Chemical Kinetics of Solids, Wiley-VCH Verlag GmbH, 2007.

[33] M.G. Makowska, M. Strobl, E.M. Lauridsen, H.L. Frandsen, A.S. Tremsin, N. Kardjilov, I. Manke, J.F. Kelleher, L.T. Kuhn, J.Appl.Crystallogr. 48 (2015) 401-408.

[34] K. Kwok, P.S. Jørgensen, H.L. Frandsen, (2014) 55-64.

[35] M. Mori, T. Yamamoto, H. Itoh, H. Inaba, H. Tagawa, J.Electrochem.Soc. 145 (1998) 1374-1381.

[36] B. Charlas, C. Chatzichristodoulou, K. Brodersen, K. Kwok, P. Norby, M. Chen, H.L. Frandsen, (2014) 44-54.

[37] D.W. Ni, B. Charlas, K. Kwok, T.T. Molla, P.V. Hendriksen, H.L. Frandsen, Journal of Power Sources, (2016) 311, 1-12.

[38] Z. Deng, J. Yang, Y. Beppu, M. Ando, T. Ohji, J Am Ceram Soc. 85 (2002) 1961-1965.

[39] B. Sun, R.A. Rudkin, A. Atkinson, Fuel Cells. 9 (2009) 805-813.

[40] Jeangros Q, Hansen TW, Wagner JB, Damsgaard CD, Dunin-Borkowski RE, Hébert C, et al., J Mater Sci 2013;48:2893–907.

[41] Frandsen HL, Chatzichristodoulou C, Hendriksen PV. (2015) In: Cigolotti V, Barchiesi C, Chianella M, editors. Proc. EFC2015, Naples, Italy: ENEA, 2015.

[42] Ebbesen SD, Mogensen M. Kinetics of Oxidation of H2 and Reduction of H2O in Ni-YSZ based Solid Oxide Cells. ECS Trans 2013;50:167–82.

[43] Makowska MG. In-situ Neutron Imaging of Solid Oxide Fuel Cells, Chapter 8. Technical University of Denmark, 2016.

[44] Jørgensen PS, Ebbehøj SL, Hauch A. Triple phase boundary specific pathway analysis for quantitative characterization of solid oxide cell electrode microstructure. J Power Sources 2015;279:686–93.

[45] Jørgensen PS, Bowen JR. Determination of Three Dimensional Microstructure Parameters from a Solid Oxide Ni/YSZ Electrode after Electrolysis Operation. ECS Trans 2011;35:1689–99.

[46] Hauch A, Jørgensen PS, Brodersen K, Mogensen M. Ni/YSZ anode - Effect of pre-treatments on cell degradation and microstructures. J Power Sources 2011;196:8931–41.

[47] Hauch a., Ebbesen SD, Jensen SH, Mogensen M. Solid Oxide Electrolysis Cells: Microstructure and Degradation of the Ni/Yttria-Stabilized Zirconia Electrode. J Electrochem Soc 2008;155:B1184.

Appendix A: Power Law Beam Theory

In a beam the Bernoulli assumption of the strain field is linear function of *y* can be applied with good approximation $\varepsilon = -\kappa y$ where κ is the curvature. Thus, the strain field can be expressed as

$$\dot{\varepsilon} = -\dot{\kappa} y = -\frac{1}{E_c}\operatorname{sgn}(\sigma)\,|\sigma|^n \tag{10}$$

Solving this equation for the stress provides

$$\sigma = -\sqrt[n]{E_c}\,\operatorname{sgn}(\dot{\kappa} y)\sqrt[n]{|\dot{\kappa} y|} \tag{11}$$

For small displacements the bending moment can be obtained by integration over the height of the beam

$$M = -w\int_{-h/2}^{h/2} \sigma y\, dy = w\sqrt[n]{E_c}\,\operatorname{sgn}(\dot{\kappa})\sqrt[n]{|\dot{\kappa}|}\int_{-h/2}^{h/2} \operatorname{sgn}(y)\sqrt[n]{|y|}\, y dy \tag{12}$$

As *M* and $\dot{\kappa}$ have the same sign Eq. (12) can be solved for $\dot{\kappa}$ to

$$\dot{\kappa} = \mathrm{sgn}(M)\left(\frac{|M|}{I_c}\right)^n \frac{1}{E_c} \tag{13}$$

where I_c is a geometric stiffness factor, which replaces the second moment (I=wh^3/12) in elastic beam theory, and for the Power Law constitutive law becomes a n^{th} moment of area

$$I_c = w\int_{-h/2}^{h/2} \mathrm{sgn}(y)\sqrt[n]{|y|}\, y dy = 2w\int_0^{h/2} |y|^{\frac{1+n}{n}}\, dy = \frac{2wn}{1+2n}\left(\frac{h}{2}\right)^{\frac{1+2n}{n}} \tag{14}$$

Notice for a linear creep law (n=1) the I_c becomes wh^3/12 as in linear elastic beam theory. This is not the case with the very similar expression in [16].

Appendix B: Creep deformation rate in three-point bending

Due to symmetry deformations can be derived by considering the left half of the beam, i.e. for $x \leq L/2$ as the left corner is located a x=0. Standard equilibrium conditions provide the shear force, Q, and bending moment, M, for three-point bending to be F/2 and -Fx/2, respectively, where F is the applied load and L the span. Inserting the bending moment in Eq. (13) provides

$$\dot{\kappa} = -\mathrm{sgn}(F)\left(\frac{|F|x}{2I_c}\right)^n \frac{1}{E_c} \tag{15}$$

Integrating the curvature provides the rotation rate of the beam, θ

$$\dot{\theta} = \int \dot{\kappa} dx = -\frac{\mathrm{sgn}(F)}{n+1}\left(\frac{|F|x}{2I_c}\right)^n \frac{1}{E_c} x + c_1 \tag{16}$$

where c_1 is an integration variable, which can be obtained from the boundary condition of the rotation (and thus also its rate) is zero at the center of the beam to

$$c_1 = \frac{\mathrm{sgn}(F)}{n+1}\left(\frac{|F|L}{2^2 I_c}\right)^n \frac{L}{2}\frac{1}{E_c} \tag{17}$$

The rotation rate can then be expressed as

$$\dot{\theta} = \frac{\mathrm{sgn}(F)}{n+1}\left(\frac{|F|}{2I_c}\right)^n \frac{1}{E_c}\left(\left(\frac{L}{2}\right)^{n+1} - x^{n+1}\right) \tag{18}$$

Integrating the rotation rate provides the displacement rate

$$\dot{v} = \int \dot{\theta}\, dx = \frac{\mathrm{sgn}(F)}{n+1}\left(\frac{|F|}{2I_c}\right)^n \frac{1}{E_c}\left(\left(\frac{L}{2}\right)^{n+1} x - \frac{1}{n+2}x^{n+2}\right) + c_2 \tag{19}$$

where c_2 is an integration variable which is zero due to the boundary condition of vertical displacements equaling zero at the supports.

Finally, the displacement rate along the beam axis and over time can be obtained

$$\dot{v} = \frac{\mathrm{sgn}(F)}{n+1}\left(\frac{|F|}{2I_c}\right)^n \frac{1}{E_c}\left(\left(\frac{L}{2}\right)^{n+1} x - \frac{1}{n+2}x^{n+2}\right) \tag{20}$$

The maximum displacement rate at the center $x=L/2$ is then

$$\dot{v}^{\max} = \frac{\mathrm{sgn}(F)}{n+2}\left(\frac{|F|}{2I_c}\right)^n \frac{1}{E_c}\left(\frac{L}{2}\right)^{n+2} \tag{21}$$

Notice for n=1 $\dot{v}^{\max} = FL^3/(48E_cI_c)$, which corresponds to the linear elastic solution. At a constant load level integration over time easily provides the displacement

$$v^{\max} = \int_0^t \dot{v}^{\max}\, dt = \frac{\operatorname{sgn}(F)}{n+2}\left(\frac{|F|}{2I_c}\right)^n \frac{1}{E_c}\left(\frac{L}{2}\right)^{n+2} t \tag{22}$$

Tables

Table 1 Loading and reduction conditions of the various uniaxial tension experiments and the observations shown in Figure 2a.

Sample #	Load and reduction sequence	Observation
1	is loaded 10 hours before the reduction initiation	Sample 1 has been exposed to primary creep, and is well into the regime of secondary creep from the current loading in the oxidized condition. Thus, the significant amount of accelerated creep that it experiences during reduction is not influenced by the primary creep in the oxidized state. The accelerated creep during the reduction does however show reminiscences of primary creep as the creep rate reduces strongly with time.
2	is reduced for 10 minutes and then loaded	Sample 3 creeps much less than sample 2, which is not fully reduced at the time of the load introduction. Thus, the sample does not need to be loaded at the very beginning of the reduction process for the accelerated creep to occur, but most of the accelerated creep has ceased after 5 minutes (see also Figure 2c).
3	is reduced for 3 hours and then loaded	

4	is the leached support (pure YSZ) loaded 10 hours before the reduction initiation	Accelerated creep is not observed in the pure YSZ sample.
5	is only exposed to oxidizing environment (air) and loaded at t=0 (as a reference)	The amount of creep in the non-reduced sample 5 is much lower than in the Ni-YSZ samples, which is to be expected because of the relatively lower creep rate of NiO compared to the Ni.

Table 2 Creep parameters of the anode support in reference from four-point bending (4pb) [16] and in this works, three-point bending (3pb) experiments and uniaxial tension (ua) experiments at 800°C.

Material state	E_c [$MPa^n s$]	n	Ref
Reduced	$3.8 \cdot 10^{10}$	1.7	4pb, [16]
In reduction	$4.5 \cdot 10^{6}$	0.8	3pb, this work
Reduced	$4.1 \cdot 10^{11}$	1.9	3pb, this work
Oxidized	$1.7 \cdot 10^{9}$	1*	ua 2.0 MPa, this work
Pure YSZ	$1.1 \cdot 10^{9}$	1*	ua 2.0 MPa, this work
In reduction	$1.0 \cdot 10^{5}$	0.8**	ua 2.0 MPa, this work
In reduction	$6.2 \cdot 10^{4}$	0.8**	ua 5.0 MPa, this work

*) assumed

**) assumed given the results of the three-point bending experiments